

# Nonadditive Interactions Unlock Small-Particle Mobility in Binary Colloidal Monolayers

Jonathan G. Raybin, Rebecca B. Wai, and Naomi S. Ginsberg\*

Cite This: *ACS Nano* 2023, 17, 8303–8314

Read Online

ACCESS |



Metrics &amp; More

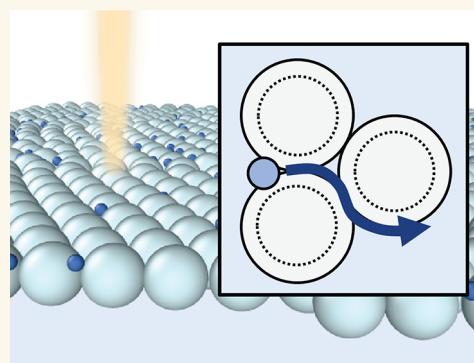


Article Recommendations



Supporting Information

**ABSTRACT:** We examine the organization and dynamics of binary colloidal monolayers composed of micron-scale silica particles interspersed with smaller-diameter silica particles that serve as minority component impurities. These binary monolayers are prepared at the surface of ionic liquid droplets over a range of size ratios ( $\sigma = 0.16$ – $0.66$ ) and are studied with low-dose minimally perturbative scanning electron microscopy (SEM). The high resolution of SEM imaging provides direct tracking of all particle coordinates over time, enabling a complete description of the microscopic state. In these bidisperse size mixtures, particle interactions are nonadditive because interfacial pinning to the droplet surface causes the equators of differently sized particles to lie in separate planes. By varying the size ratio, we control the extent of nonadditivity in order to achieve phase behavior inaccessible to additive 2D systems. Across the range of size ratios, we tune the system from a mobile small-particle phase ( $\sigma < 0.24$ ) to an interstitial solid ( $0.24 < \sigma < 0.33$ ) and furthermore to a disordered glass ( $\sigma > 0.33$ ). These distinct phase regimes are classified through measurements of hexagonal ordering of the large-particle host lattice and the lattice's capacity for small-particle transport. Altogether, we explain these structural and dynamic trends by considering the combined influence of interparticle interactions and the colloidal packing geometry. Our measurements are reproduced in molecular dynamics simulations of 2D nonadditive disks, suggesting an efficient method for describing confined systems with reduced dimensionality representations.



**KEYWORDS:** colloids, soft condensed matter, electron microscopy, interfacial assembly, ionic liquid, nanoparticles, nonadditivity

## INTRODUCTION

Colloidal nanoparticles serve as versatile building blocks for the self-assembly of nanostructured materials, due to the tunability of their material, size, shape, and surface chemistry.<sup>1,2</sup> Combining multiple colloidal components introduces additional length and energy scales that further expand the scope of possible structures.<sup>3–5</sup> Even in the relatively simple case of two-dimensional (2D) binary mixtures of differently sized spheres, particle assemblies exhibit a diverse array of morphologies, including crystalline,<sup>6,7</sup> quasicrystalline,<sup>8–10</sup> and amorphous phases.<sup>11</sup> In general, the assembly process is governed by a range of competing kinetic and thermodynamic effects, dependent on a hierarchy of particle–particle and particle–environment interactions. Despite this overall complexity, much of the observed structural diversity can be generated from simplified model systems of hard disks interacting only through volume exclusion.<sup>12,13</sup>

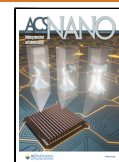
In bidisperse monolayers composed of large and small particles, with respective radii  $r_L$  and  $r_S$ , in addition to the total particle density  $\phi_T$ , the system state also depends on the binary

number fraction  $\chi_S = 1 - \chi_L$  and size ratio  $\sigma = r_S/r_L$ . Additionally, in many binary mixtures, the pairwise interaction length scale  $2r_{LS}$  does not necessarily correspond to the additive sum of the component radii,  $r_L + r_S$ . To account for this difference, binary hard-disk models may be generalized by incorporating a nonadditivity term  $\Delta$  such that  $r_{LS} = \frac{1}{2}(r_L + r_S)(1 + \Delta)$ .<sup>14</sup> Positive nonadditivity introduces an effective interspecies repulsion and can lead to phase separation, while negative nonadditivity generates an effective attraction that promotes mixing. In experimental systems, nonadditivity frequently arises from soft interactions due to particle charge, surface chemistry, solvation, or ligand

Received: December 22, 2022

Accepted: April 19, 2023

Published: April 24, 2023



intercalation.<sup>15</sup> For example, the widely applied Asakura–Oosawa model for depletion interactions in polymer–colloid mixtures assumes no interaction between the polymer chain depletants and represents a limiting case of positive nonadditivity.<sup>16</sup> In addition to hard-core models, analogous nonadditivity relations have been developed for soft potentials, including electrostatic interactions between differently sized charged colloidal particles. In each of these cases, an accurate understanding of the effects of nonadditivity is critical, as nonadditive mixtures access distinct structural phases with unique material properties.<sup>13,17</sup> Nonadditive interactions have also recently been proposed as a design mechanism for the programmed self-assembly of monolayers with controlled open lattice architectures.<sup>18</sup>

Interfacially confined monolayers serve as a natural platform for studying nonadditivity in 2D systems. Whether sedimented at a solid interface or adsorbed to a fluid interface, the equators of spheres of different sizes lie at different levels from the surface. The resulting height offset leads to an effective shortening of the minimum approach distance between large and small spheres when projected onto the plane in which they make contact. Meanwhile, particles of the same size lie in a common plane, and their contact distances remain unchanged. Consequently, under the confined geometry, particle interactions may be described following a 2D nonadditive representation. Following these arguments, several recent studies have simulated hard-disk mixtures with negative nonadditivity to analyze the phase behavior of confined nanospheres.<sup>10,13,18</sup> To our knowledge, however, the effect of nonadditivity on binary assembly at interfaces has not been examined experimentally. Although the assembly and dynamics of binary colloidal monolayers have been extensively studied,<sup>11,19–26</sup> these investigations have considered only single size ratios or have focused on size ratio regimes where the effects of nonadditivity may be neglected.

Here, we systematically measure the structural and dynamic properties of bidisperse mixtures of interfacially confined silica nanospheres over a range of size ratios. Despite the inherently 3D geometry, we demonstrate that the monolayer may be represented as a 2D system of nonadditive particles. Over this series, nonadditivity, which is enhanced with increasing size asymmetry, plays an essential role in determining monolayer properties. For example, at low size ratios, we observe a mobile small-particle phase exhibiting delocalized transport properties that would be inaccessible to additive 2D systems. We also find that nonadditivity reduces lattice strain, leading to improved structural ordering of the large particles over a broader range of size ratios. Although we obtain evidence for additional interparticle interactions beyond area exclusion, we find that a simple nonadditive hard-disk model is sufficient for explaining the observed phase behavior. Altogether, these observations can be understood from 3D geometric packing arguments resulting from interfacial confinement.

## RESULTS

We used scanning electron microscopy (SEM) to image colloidal monolayers comprising bidisperse mixtures of silica nanospheres with varying size ratios ( $\sigma = 0.16$ – $0.67$ ). Figure 1a illustrates the imaging geometry, with colloidal monolayers organized at a droplet surface. For these experiments, we suspend the particles on ionic liquid droplets, as the low vapor pressure allows for direct compatibility with the SEM vacuum environment.<sup>11,27–29</sup> Prior to imaging, droplets are allowed to

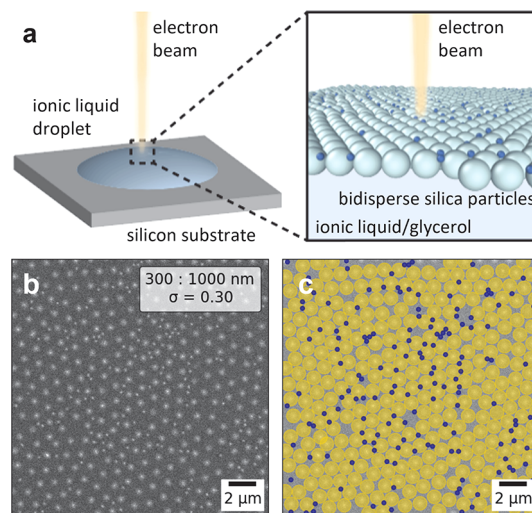


**Figure 1.** Scanning electron microscopy (SEM) monolayer imaging. (a) Experimental schematic showing assembly of binary nanospheres at the interface of an ionic liquid droplet with the electron beam scanning over the monolayer. (b) Representative SEM image of a binary monolayer and (c) the same image labeled with space-filling circles showing the full particle sizes projected onto a 2D plane, as measured through automated particle tracking.

equilibrate for at least 12 h under an inert environment to facilitate the formation of dense monolayer assemblies. Following equilibration, particles collect around the droplet center in a single, large-area ( $\sim 1 \text{ mm}^2$ ) patch with consistent density, surrounded by dilute particles at the periphery of the droplet. Increasing the particle concentration increases the size of this patch, and we do not find evidence for the formation of multilayers or colloidal aggregation below the monolayer surface. Within the high-density patch, particles saturate at the interface with total surface coverage fractions of  $\phi_T = 0.76 \pm 0.04$ , calculated as  $\phi_T = \phi_L + \phi_S - \phi_{LS}$ , where  $\phi_i$  is the surface coverage of each component  $i = L$  or  $S$ , and  $\phi_{LS}$  represents the large-small area overlap. Although the local composition varies across the monolayer surface, all presented imaging regions were selected with small-particle number fractions  $\chi_S = 0.29 \pm 0.04$ , except where otherwise noted. These conditions correspond to dense, large-particle majority lattices where the small particles act as minority component impurities. Following their initial assembly, the high density of particle contacts hinders further rearrangements such that the resulting monolayers remain kinetically trapped in configurations that are locally stable but outside of global equilibrium. Still, average monolayer properties are consistent across regions with the same local composition and are reproducible over multiple droplet samples.

SEM imaging ensures sufficient spatial and temporal resolution to directly locate all 2D particle coordinates over time. For each size ratio, we measured time-resolved movies of particle dynamics in the monolayer with 2.1 s time resolution. We also separately acquire multiple images of the initial particle configuration over larger fields of view to assess the monolayer structure. In each of these experiments, we use a very low 15 pA beam current for minimally perturbative imaging. In this regime, particle charging from the cumulative electron dose preserves monolayer stability for roughly 2 min, which is more than sufficient for acquiring dynamic information at each pristine sample region of interest. At this

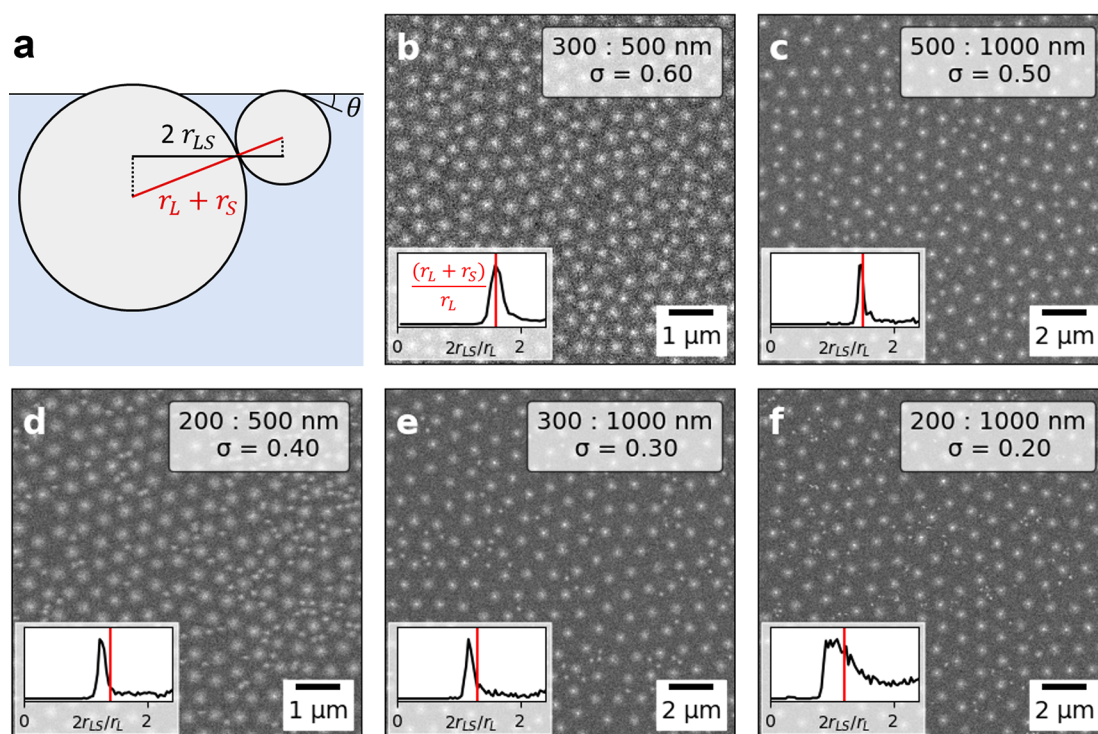


**Figure 2.** Bidisperse monolayer images over varying size ratio. (a) Schematic of the nonadditive interfacial geometry showing large and small particles attached to the interface with the same contact angle  $\theta$ . The full center-to-center distance  $r_L + r_S$  (red) is greater than the 2D projected center-to-center distance  $2r_{LS}$  (black). (b–f) Representative monolayer images with consistent  $\chi_S = 0.29 \pm 0.05$  over a series of size ratios (b) 0.60, (c) 0.50, (d) 0.40, (e) 0.30, and (f) 0.20. Insets for each image plot the measured distributions of pairwise large-small separations  $2r_{LS}$  (black curve) compared to the additive particle radii  $r_L + r_S$  (red vertical line), measured in units of the large-particle radius.

low beam dosage, we observe no changes in contrast or imaging artifacts due to particle charging over the course of imaging. Further discussion of the effects of perturbation is included in the Supporting Information (Figure S1). A representative secondary electron image of a 300 nm/1000 nm binary mixture is shown in Figure 1b. These images were acquired with an accelerating voltage of 3 kV, such that all particles are clearly resolved and that large and small particles can be distinguished by automated particle tracking. At their equilibrium contact angle, surface-bound particles are almost entirely submerged below the liquid interface, and secondary electrons scatter from only their upper cap region.<sup>27,29</sup> Although the particles appear to be spatially separated, labeling the image with space-filling radii for the large (yellow) and small (blue) particles in Figure 1c reveals direct contacts between particles. Imaging at higher accelerating voltages probes greater depths and further confirms that particles are in close contact below the ionic liquid surface, as seen in Figure S2.

**Control over Nonadditivity.** In bidisperse monolayers, large and small particles, with respective radii  $r_L$  and  $r_S$ , are pinned with identical contact angles to the droplet surface, displacing their equatorial planes relative to one another. As shown in Figure 2a, this configuration causes the projected top-down contact distances of large and small particles  $2r_{LS}$  to be shorter than the additive sum of their radii  $r_L + r_S$ . Representative SEM images over a series of size ratios are shown in Figure 2b–f, with absolute particle size ranging from 200 nm to 1  $\mu$ m. Note that the images shown have been extracted from larger fields of view and scaled such that the large particles have similar apparent sizes. Across the full range of size ratios, monolayers form densely packed assemblies with

direct contacts between most neighboring particles. Inset plots show the distribution of measured separation distances for each large-small neighbor pair as compared to the additive sum. Particle separations show broad, asymmetric distributions as not all large-small pairs reflect direct contacts, but particles cannot approach closer than the contact distance; this broadening is particularly evident at the smallest size ratios where there is more free space in the interstices between large particles. In general, the peak value of  $2r_{LS}$  is smaller than  $r_L + r_S$ , and the relative difference between these two quantities increases with increasing size asymmetry as the system becomes more nonadditive.

This trend is reflected in observations of overlapping large and small particles in the projected 2D images. An example is shown for a  $\sigma = 0.16$  monolayer with higher small-particle number fraction  $\chi_S$  in Figure 3a,b, where small particles fill the interstitial space between large particles. From measurements of  $r_{LS}$ , the nonadditivity parameter may be quantified as

$$\Delta = \frac{2r_{LS}}{r_L + r_S} - 1 \quad (1)$$

In the case of overlapping particles the nonadditivity  $\Delta$  is negative. From direct measurements of  $r_{LS}$  across multiple imaging regions, we determine nonadditivity distributions for monolayers of each size ratio, as shown in Figure 3c. For these measurements, images with local compositions of  $\chi_S > 0.50$  were used for systems with  $\sigma \leq 0.3$  to ensure adequate small-large contact statistics. The peak positions of the resulting distribution are most negative at low  $\sigma$  and approach 0 with decreasing size asymmetry. Across the range of measured size



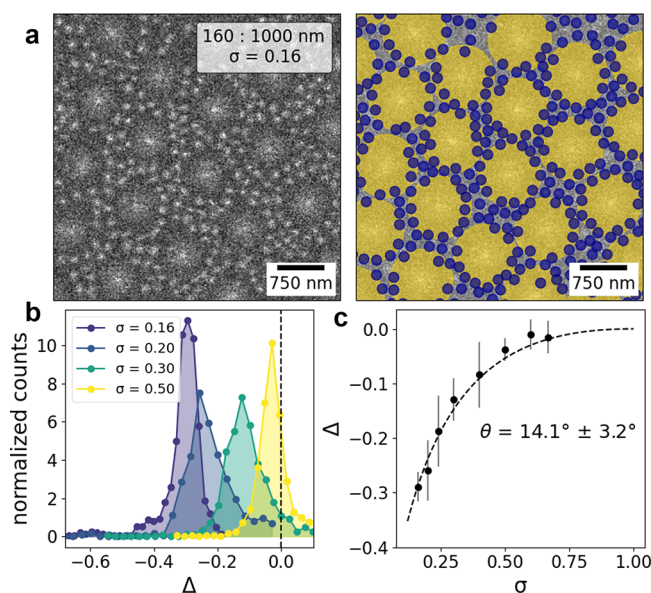


**Figure 3. Nonadditivity quantification.** (a) SEM image showing particle overlap in a  $\sigma = 0.16$  monolayer with  $\chi_s = 0.93$  and the same image labeled with space-filling circles. (b) Histograms showing the shift of measured nonadditivity distributions with increasing size ratio. (c) Plot of  $\Delta$  as a function of size ratio. The contact angle is measured from fitting to eq 2 as indicated by the dashed black curve.

ratios, nonadditivity may be tuned from  $\Delta = -0.29 \pm 0.03$  at  $\sigma = 0.16$  to  $\Delta = -0.02 \pm 0.03$  at  $\sigma = 0.67$ .

The peak positions of  $\Delta$  are plotted as a function of  $\sigma$  in Figure 3d, with uncertainties corresponding to the full widths at half-maximum. Under the assumption that large and small silica particles attach to the interface with the same contact angle  $\theta$ , the nonadditivity may be determined geometrically as a function of the size ratio and contact angle:

$$\Delta = \sqrt{1 - \frac{(\sigma - 1)^2}{(\sigma + 1)^2} \cos^2 \theta} - 1 \quad (2)$$

In this expression,  $\Delta$  vanishes at the additive limit of  $\theta = 90^\circ$ , where particle centers collect at the interfacial plane. At  $\theta = 0^\circ$ , where particles lie tangent to the interface,  $\Delta$  is most negative and reduces to  $\Delta = \frac{2\sqrt{2}}{1 + \sigma} - 1$ . This limit also corresponds to the case of particle sedimentation at a rigid interface.<sup>13</sup> Our measured values of  $\Delta$  agree closely with eq 2, indicated by the black curve in Figure 3d, suggesting that the interfacial geometry shown in Figure 2a provides a descriptive model of our system. Because  $\theta$  serves as the only adjustable parameter, this fit enables an independent measure of the particle contact angle from plane-view SEM images. We estimate  $\theta = 14.1 \pm 3.1^\circ$ , consistent with previous measurements of silica nanoparticles in the same ionic liquid in the range  $\theta = 12^\circ$ – $15^\circ$ .<sup>28</sup> Consequently, this nonadditive representation serves as a practical framework for reconstructing the organization of the inherently 3D system using 2D imaging data.

**Size Ratio-Dependent Small-Particle Mobility.** Having established the relationship between nonadditivity  $\Delta$  and the binary size ratio  $\sigma$ , we investigate the influence of nonadditivity on particle mobility. Figure 4a shows experimental trajectories of large (yellow) and small (blue) particles obtained from SEM movie data over a series of three representative size ratios. At

each size ratio, large particles exhibit minimal displacements over experimental time scales due to the high density of large-particle contacts. The large-particle network therefore serves as a stable reference environment for tracking the relative dynamics of small-particle impurities. At low size ratios, as shown for  $\sigma = 0.20$ , small particles are observed to percolate through the interstices of the large-particle lattice. At the low small-particle density  $\chi_s = 0.29 \pm 0.05$  studied here, most interstitial sites are unoccupied such that small particles can travel between sites without interacting. At  $\sigma = 0.30$ , small-particle mobility is suppressed and trajectories become trapped within individual large-particle hollow-site cages. Near vacancies and defect sites in the lattice, small-particle trajectories at this size ratio explore the larger accessible free space but remain locally confined by the cage structure. With further increases in size ratio, as seen for  $\sigma = 0.60$ , small-particle mobility becomes fully restricted and yields compact, localized trajectories. In this regime, large and small particles together form a common packing network that limits the mobility of both species.

As a test of this point, we find that the observed trajectories may be recapitulated through molecular dynamics simulations of nonadditive particles with steep short-range repulsion described by the Weeks–Chandler–Andersen (WCA) potential.<sup>30</sup> At each size ratio, simulated trajectories, as shown in Figure 4b, closely resemble those of the corresponding experimental monolayer. In these simulations, the nonadditivity  $\Delta$  was determined from the binary size ratio following eq 2 with  $\theta = 15^\circ$  and introduced by shortening the interaction length scale between large and small disks. Importantly, the simulated Brownian dynamics depend only on interactions between disks and with the equilibrated bath, while neglecting any effects of electron beam perturbation. The observed agreement therefore indicates that the observed particle mobility does not rely on peculiarities of the electron beam interaction but instead depends on common structural features of the experimental and simulated monolayers.

As a measure of particle mobility, in Figure 4c, we plot the root-mean-square (RMS) displacement  $\sqrt{\langle \delta r_s^2(\tau) \rangle}$ , following evolution over a delay time  $\tau$ , over the full experimental range of size ratios. The delay time, which is further discussed in the Supporting Information, scales as  $\tau \propto r_s r_L^2$  and reflects the Brownian time scale for small-particle diffusion through the large-particle lattice environment. We also plot the fraction of small particles,  $f_{s,\text{hop}}$  that hop between lattice sites within this time window, such that  $|\delta r_s(\tau)| > 2r_L$ . In both experiment and simulation, small-particle mobility (blue) shows a crossover from a mobile, percolating phase at low size ratios to an immobile, trapped phase at higher size ratios. The mobile phase is characterized by frequent site-to-site hopping of the small-particle impurities, leading to a divergent RMS displacement at late times. In the trapped phase, the confinement of small particles to individual sites suppresses long-range transport. For comparison, we note that the large-particle RMS displacement remains small for all size ratios and does not exceed the lattice spacing.

The enhancement in small-particle mobility can be understood by considering the nonadditive configuration of the monolayer. Small particles are able to hop between hollow sites only when they are small enough to fit between large-particle gaps at bridge sites. Because they lie in separate planes, sufficiently small particles are able to pass through the channel



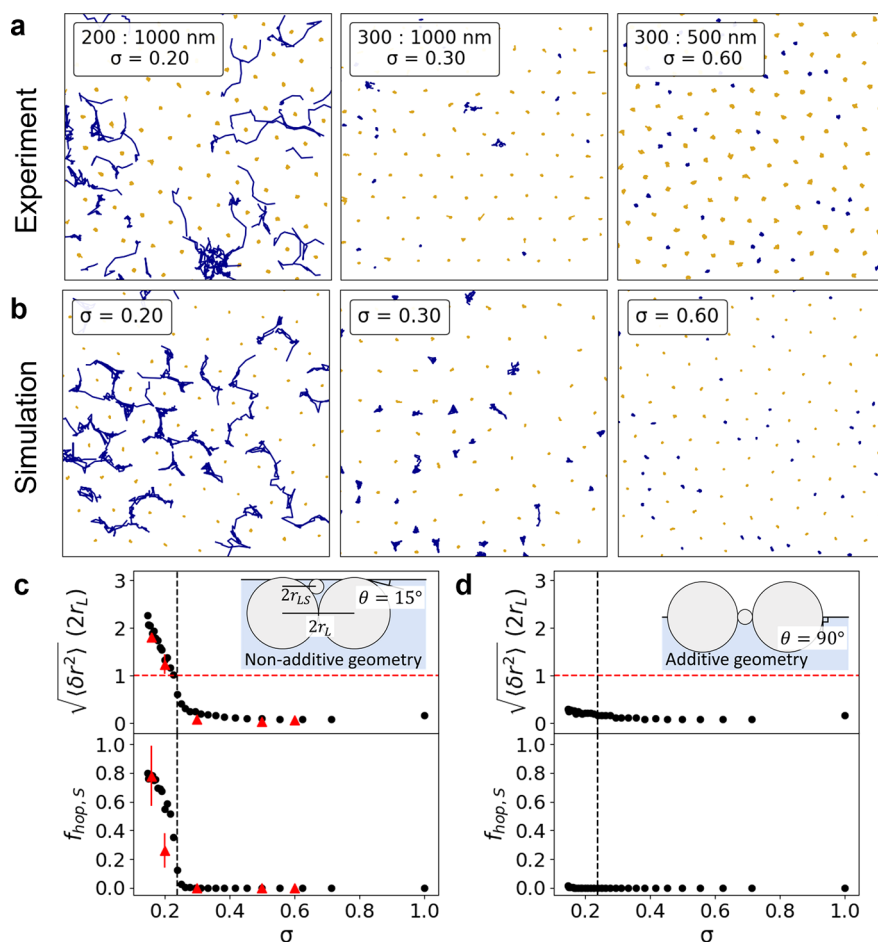


**Figure 4.** Monolayer dynamics. (a) Experimentally measured particle trajectories for a series of size ratios  $\sigma = 0.20, 0.30$ , and  $0.60$  over imaging times of 88 s. Small-particle trajectories are shown in blue, and large-particle trajectories are in yellow. (b) Trajectories measured from simulations of nonadditive WCA particles for the same size ratios. (c) Plots measuring particle dynamics as a function of size ratio based on experiment and nonadditive simulations. The inset depicts the effective nonadditive geometry used for the simulations, corresponding to a contact angle of  $15^\circ$ . The upper panel shows the RMS displacement of small particles for experiment (red triangles) and simulation (black circles) after a delay time  $\tau$ . The lower panel measures the fraction of small particles with a displacement greater than one lattice spacing. An abrupt decrease in small-particle mobility is observed as  $\sigma$  increases past  $0.24$ , indicated by the dashed vertical line. (d) Similar plots measuring the dynamics of simulated additive disks. The inset shows the effective geometry of the additive system, corresponding to a contact angle of  $90^\circ$ . No small-particle mobility crossover is observed in additive simulations.

formed above the large-particle contact point. As depicted in the inset of Figure 4c, this criterion is satisfied when  $r_{LS} < r_L/2$ . Through substitution from eq 1, we obtain

$$(1 + \sigma)(1 + \Delta) < 1 \quad (3)$$

Because of the well-defined functional relationship between  $\sigma$  and  $\Delta$  in eq 2, we can fully parameterize this inequality in terms of  $\sigma$ , obtaining a numerical threshold of  $\sigma \sim 0.24$  for this system, as indicated by the dashed vertical line in Figure 4c, in close agreement with the observed crossover point.

Following this model, the predicted crossover is a direct consequence of the nonadditive geometry. Notably, there is no solution to the inequality in eq 3 in the case of  $\Delta = 0$ , suggesting that the observed mobile phase is inaccessible to strictly planar systems. Previous investigations have found that particle motion becomes increasingly hindered with increasing surface coverage, approaching kinetic arrest in the dense limit.<sup>24,31,32</sup> To better understand the effects of nonadditivity, we repeated the colloidal simulations using *additive* WCA particles across the full range of size ratios. As shown in the inset of Figure 4d, the additive system corresponds to a

monolayer geometry with  $\theta = 90^\circ$  where all particles are attached to the interface at the same plane. In the plots, no crossover to a mobile phase is seen in measurements of either the RMS displacement or  $f_{\text{hop},s}$  in the additive simulations. We still observe a marginal increase in the small-particle RMS displacement at low size ratios due to the expanded free area for small particles to explore within each hollow site, but displacements plateau at late times and do not exceed the lattice spacing. In the additive geometry, small particles are no longer able to slide over the gaps between large particles, and contact points therefore obstruct hopping pathways between hollow sites, restricting small-particle mobility for all size ratios.

**Packing Constraints for Large-Particle Ordering.** The structure of the underlying large-particle lattice environment defines the landscape for small-particle dynamics. In the absence of small particles, a monodisperse collection of nanoparticles at the fluid interface assembles to form a hexagonal lattice that maximizes surface density, as shown in Figure S3. During monolayer formation, the concurrent nucleation of multiple crystalline domains results in a polycrystalline structure with competing grain orientations.

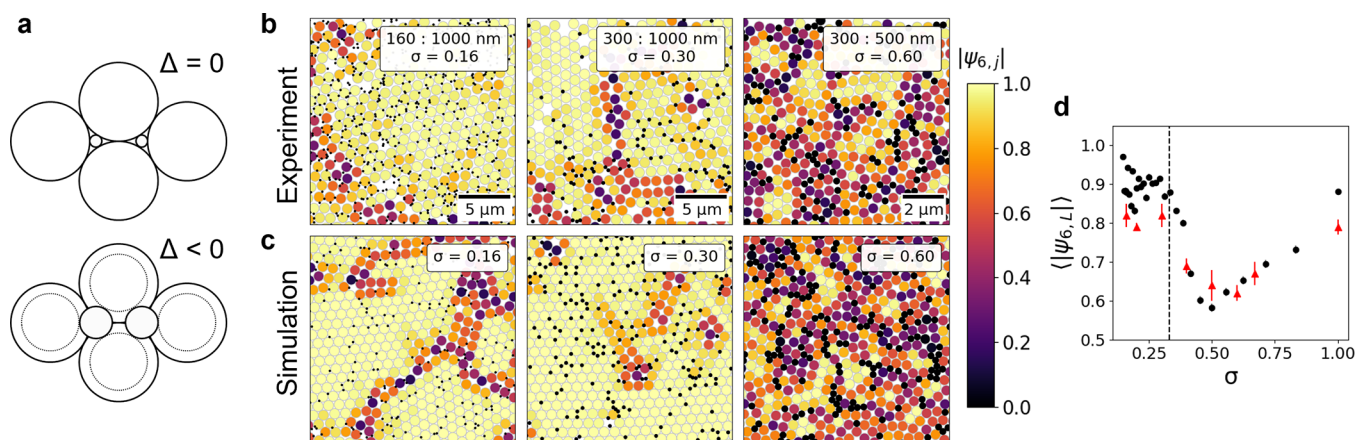


**Figure 5.** Lattice structure measurements. (a) Close-packed configuration of interstitial impurities of additive ( $\Delta = 0$ ) and nonadditive packing geometries ( $\Delta < 0$ ). (b) Bidisperse monolayer images over a series of three size ratios  $\sigma = 0.16, 0.30$ , and  $0.60$ , with the large particles false colored by the magnitude of the hexagonal bond order parameter  $|\Psi_{6,j}|$  and small particles colored black. (c) Snapshots of simulated nonadditive WCA particles at the same size ratios as in (b). (d) Plot of the average large-particle hexagonal order  $\langle |\Psi_{6,L}| \rangle$  as a function of size ratio measured from experiment (red triangles) and simulation (black circles).

For mixtures including small particles, the question of optimal 2D packing becomes significantly more complex, and a wide variety of close-packed configurations exists depending on the composition and size ratio of the mixture. In practice, we do not obtain true close-packed structures as the propensity for maximizing surface coverage is mitigated by thermal fluctuations, interparticle interactions, and kinetic trapping, among other factors. Still, close-packing remains a useful heuristic, and to describe our observations, we pay special attention to the packing geometry where a single small particle fits exactly within the interstices of hexagonally packed large particles, as depicted in Figure 5a. We focus on this case as it accommodates the small-particle impurities while preserving the hexagonal symmetry of the large-particle sublattice. For additive systems, this packing occurs at a so-called “magic” size ratio of  $\sigma = \frac{2}{\sqrt{3}} - 1 \approx 0.15$  that corresponds to the case where  $2r_{LS}$  is equal to the distance between the center and vertex points of an equilateral triangle with side length  $2r_L$ .<sup>33</sup> In nonadditive systems, similar packing rules apply, but particle overlap allows larger particles to fit within the interstitial space, introducing a correction factor to  $r_{LS}$ , resulting in a magic ratio that we derived as

$$(1 + \sigma)(1 + \Delta) = \frac{2}{\sqrt{3}} \quad (4)$$

Substituting eq 2, into this expression and using  $\theta = 15^\circ$  we obtain a numerical threshold of  $\sigma \sim 0.33$  for nonadditive close-packing. Thus, negative nonadditivity shifts the stability of this close-packed configuration to higher values of  $\sigma$ .

In close-packed systems, when the size ratio deviates from this “magic” value, shear deformation of the large-particle sublattice leads to a reduction of hexagonal symmetry.<sup>33</sup> We quantify the extent of deformation by measuring the large-particle hexagonal bond order parameter  $\Psi_{6,j}$ , defined for each large particle  $j$  as

$$\Psi_{6,j} = \frac{1}{N_{nn}} \sum_{k=1}^{N_{nn}} e^{6i\theta_k} \quad (5)$$

where  $N_{nn}$  is the number of nearest neighbor particles and  $\theta_k$  is the angle of the bond vector linking to the  $k$ -th neighbor. For

this calculation, nearest neighbors are uniquely defined through Delaunay triangulation of the large-particle coordinates with a maximum center-to-center separation of  $3r_L$ . The order parameter is complex valued, such that the magnitude  $|\Psi_{6,j}|$ , ranging from 0 to 1, indicates the degree of local hexagonal order, while the phase corresponds to the grain orientation. Figure 5b compares large-particle order in experimental monolayers over a series of three size ratios. In each panel, large particles are colored according to their individual  $|\Psi_{6,j}|$ ; small particles are not included for this analysis and have been colored black. Snapshots taken from equilibrated simulations for these size ratios display similar structural organization, as shown in Figure 5c. In the  $\sigma = 0.16$  and  $0.30$  examples, which fall below the threshold size ratio for close packing, large particles form an ordered polycrystalline monolayer, with ordered domains separated by disordered grain boundaries. The organization of the lattice in the  $\sigma = 0.30$  case, just below the threshold, does not differ significantly from that of  $\sigma = 0.16$ . In both cases, the structure of the large-particle sublattice is not disrupted by the inclusion of small particles and resembles monodisperse assembly. The lattice accommodates small particles within vacant interstitial hollow sites while preserving the underlying hexagonal symmetry. By contrast, in the  $\sigma = 0.60$  monolayer, we find that the ordering of large particles is significantly disrupted. In this regime, deformation is unavoidable, and hexagonal packing is frustrated by the presence of small particles. The monolayer maintains direct contacts between neighboring particles, resulting in a generally amorphous random close-packed structure. Although the system exhibits no long-range order, patchy crystallite grains with local hexagonal symmetry are distributed throughout the monolayer, corresponding to regions that exclude small particles.<sup>20</sup>

To assess structural properties across the full range of size ratios, in Figure 5d, we average over all large particles to obtain the mean magnitude  $\langle |\Psi_{6,L}| \rangle$  for each monolayer. Experimental uncertainties indicate the image-to-image standard deviation for different fields of view of the same ionic liquid droplet surface. In both experiment and simulation, we observe a sharp decrease in hexagonal order crossing over the threshold size ratio of  $\sigma \sim 0.33$ . At  $\sigma < 0.33$  where small particles are able to occupy the interstitial space,  $\langle |\Psi_{6,L}| \rangle$  remains relatively



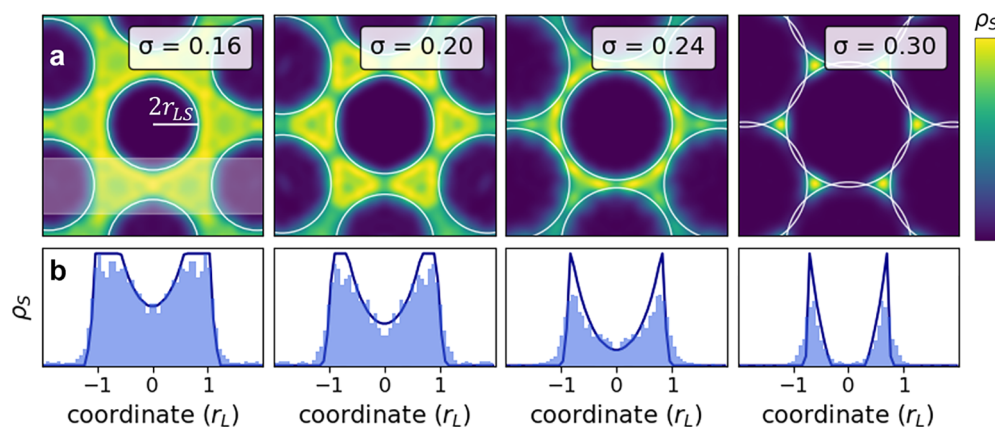


**Figure 6.** Small-particle distribution maps. (a) Real-space maps showing the spatial distribution of small particles averaged over ordered large-particle lattice sites for a series of size ratios  $\sigma = 0.30, 0.24, 0.20$ , and  $0.16$ . The color-scale indicates the local probability density of small particles, with yellow being high density and blue being low density. Small-particles occupy large-particle lattice interstices and are found to be excluded from circles with a radius  $2r_{LS}$  centered on large particle centers, with the borders of the excluded area indicated by white circles. (b) Density maps projected along the hopping coordinate between two lattice sites, as indicated by the annotated region in the first panel of (a). These plots compare the measured small-particle density (pale blue) from (a) to the total interstitial free area (dark blue) as determined from the area of the excluded lattice sites.

constant at a value comparable to monodisperse packing. This phase resembles a quasi-2D interstitial solid solution with partial occupation of lattice sites.<sup>4</sup> Although the hexagonal order achieved in simulation at  $\sigma < 0.33$  is systematically higher than in experiment due to the formation of larger polycrystalline grains, the similarity of ordering to monodisperse packing in each case confirms the absence of strain due to small-particle impurities. For  $\sigma > 0.33$ ,  $\langle |\Psi_{6L}| \rangle$  sharply decreases reaching a minimum at  $\sigma \sim 0.50$  and then gradually increases approaching monodispersity. Small particles no longer fit within the interstitial hollow of three large particles, and deformation of the large-particle lattice is unavoidable. At size ratios approaching  $\sigma = 1.0$ , small particles can act as substitutional impurities in the hexagonal lattice, similarly relaxing lattice frustration for mixtures with low size asymmetry.

**Static Distributions Predict Small-Particle Mobility.** In monolayers with size ratios below  $\sigma \sim 0.33$ , small-particle impurities are distributed throughout the interstices of the ordered large-particle sublattice. In this regime, small particles do not contribute to the mechanical stability of the monolayer, as they are not large enough to be in contact with each of their immediate large-particle neighbors. As observed in our mobility measurements, they are therefore free to move within the interstitial space, occupying a range of positions in the empty region defined by the large-particle lattice.<sup>34</sup> At size ratios below  $\sigma \sim 0.24$  the extent of small-particle motion increases further due the opening of continuous transport pathways for percolation. Real-space maps of the small-particle probability density  $\rho_s$  are generated by plotting the experimentally measured small-particle positions relative to a central large particle, rotated to obtain a consistent unit cell orientation. Small-particle positions are then mapped over each large-particle lattice hollow site to account for the 6-fold rotational symmetry of the lattice. By accumulating small particles over hundreds of unit cells, we obtain a representative sampling of their local distribution, and the resulting  $\rho_s$  maps are plotted in Figure 6a. The full details of this analysis are discussed in the Supporting Information and presented in Figure S4. Because distributions are measured using the first

SEM image obtained on each region, we do not expect SEM charging or other imaging artifacts to have influenced the particle configuration.

Figure 6a shows that at each size ratio,  $\rho_s$  is distributed within the interstitial space within volume-excluded large-particle lattice sites. White circles indicate the borders of the excluded area inaccessible to small-particle centers, extending a distance  $2r_{LS}$  from the large particle center in the contact plane. In the  $\sigma = 0.16$  monolayer, hollow sites are joined by continuous open pathways enabling free transport of small particles. At this size ratio, the significant height offset between large and small particles effectively lowers the overall particle density in the contact plane. With increasing size ratio,  $r_{LS}$  increases, expanding the excluded area and shrinking the pathways for small-particle percolation through lattice. In the  $\sigma = 0.30$  monolayer, the excluded area of adjacent large particles overlaps, causing  $\rho_s$  to be separated into disconnected hollow sites. Altogether, the small-particle distributions obtained from static images recapitulate the dynamics observed in SEM movies. The size ratio where the excluded area no longer overlaps and transport pathways first appear coincides with the  $\sigma \sim 0.24$  threshold determined from observations of particle dynamics. This strong correspondence between our measurements of the initial structure and the ensuing dynamics further demonstrates the capability for sensitive SEM imaging of liquid samples under minimally perturbative conditions.

To quantify transport probabilities, in Figure 6b, we compute  $\rho_s$  projected along the site-to-site hopping coordinate from the corresponding data in Figure 6a for each size ratio, *i.e.*, hops from the center of one large-particle hollow site to the next. The small-particle density distribution (pale blue) is plotted alongside the free area due to large-particle volume exclusion (dark blue), each integrated over the cross-section of the sampled region annotated by the white band in the  $\sigma = 0.16$  panel of Figure 6a. Comparison of these curves allows us to evaluate the relative contributions of geometric and nongeometric effects on the local monolayer structure. While the probability density generally follows from these geometric predictions, differences arise due to interparticle interactions and lattice dynamics. Along the hopping coordinate  $x$ ,  $\rho_s$  is

minimized at the narrowest point between large particles and is maximized at hollow sites. We therefore calculate a hopping barrier  $E_a$  for transport between sites following

$$E_a = -k_B T \ln \frac{\min(\rho_s(x))}{\max(\rho_s(x))} \quad (6)$$

where  $k_B$  is the Boltzmann constant and  $T$  is temperature. Measured activation energies increase with increasing size ratio and are included in Table 1. Notably, in the  $\sigma = 0.30$  case, we

**Table 1. Activation Energies for Small-Particle Site-to-Site Hopping**

$\sigma$	$E_a/k_B T$
0.16	$0.60 \pm 0.02$
0.20	$1.19 \pm 0.08$
0.24	$1.45 \pm 0.07$
0.30	$3.42 \pm 0.29$

observe nonzero probability for small particles along the full hopping coordinate, leading to a barrier of  $3.4 \pm 0.3 k_B T$ . The corresponding static geometric model predicts that large particles should fully obstruct the hopping pathway, resulting in an infinite barrier. In practice, this geometric constraint is relaxed due to out-of-plane fluctuations, heterogeneity between lattice sites, and the elastic response of the large-particle lattice. Additionally, dynamics of the host lattice have previously been shown to facilitate impurity transport in interstitial colloids.<sup>35</sup> Similarly, for each monolayer, we observe that distribution fringes extend a finite distance into the excluded region, effectively lowering the hopping barrier. At smaller size ratios where transport pathways are wider, this effect becomes less significant, and experimentally measured barriers converge with geometric predictions.

In a hard-disk system, where particles interact only through area exclusion, we would expect small particles to be evenly distributed over the region of accessible microstates. Instead,  $\rho_s$  shows local variability within each hollow site, with enhanced probability for small particles close to neighboring large particles. This pattern, which is most apparent in the  $\sigma = 0.20$  distribution, is indicative of short-range attractive interactions between large and small particles. We expect that these forces primarily arise from the capillary attraction of interfacially bound particles, as electrostatic interactions are effectively screened by the ionic liquid solvent.<sup>27,28</sup> While the simulations reported here rely on purely repulsive interactions, we find that the observed phase behavior is robust to the inclusion of modest attractive interactions with well depths of up to roughly  $5 k_B T$ . Simulations with stronger interparticle attraction result in irreversible aggregation and hindered dynamics. A comparison of simulation results for different interparticle potentials is included in Figure S5.

## DISCUSSION

Taken together, our dynamic and structural observations allow us to classify the bidisperse monolayers into three distinct phase regimes. Phase boundaries for these regimes are determined from the thresholds obtained from eqs 3 and 4. For  $\sigma < 0.33$ , the monolayer forms a large-particle polycrystalline lattice, where small particles are disconnected from the large-particle packing network and fluctuate within the interstitial space. Within this regime, for  $\sigma < 0.24$ , small

particles are able to percolate freely through the empty space defined by the large-particle lattice. For  $0.24 < \sigma < 0.33$ , however, the accessible space becomes partitioned into disconnected tricuspid cages, causing the range of small-particle motion to be localized within individual hollow sites. In monolayers with  $0.33 < \sigma < 0.67$ , small particles no longer fit within hollow sites and therefore establish mechanical contact with the packing network. In this range, large and small particles together form a randomly packed assembly with negligible particle mobility. Previous investigation of bidisperse monolayers with  $\sigma = 0.41$ – $0.78$  demonstrated the formation of a jammed state with no detectable particle rearrangements over several hour periods.<sup>11</sup> Mixtures in this range of size ratios are commonly employed as glass formers, characterized by amorphous structure and slow dynamic time scales.<sup>34,36</sup> Although our observations are also consistent with particle jamming, we note that experimental monolayer densities are lower than typical critical packing fractions of  $\phi_T = 0.81$ – $0.89$  for random close packing in 2D.<sup>37</sup> Altogether, this behavior is consistent with geometric predictions for the interaction of nonadditive hard disks.

Over the series of small-/large-particle ratios studied, nonadditivity plays an essential role in determining the observed phase behavior. In particular, the small-particle mobility crossover relies on the formation of a continuous interstitial matrix for small-particle percolation. Such interconnectivity is only possible when small particles are able to slide through the void space between large particles and is therefore inaccessible to additive systems. While enabled by the underlying large-particle lattice structure, the enhanced small-particle mobility also influences the organization of the large particles. Because differently sized particles interact in separate contact planes, nonadditivity effectively decouples their dynamics, allowing for reconfiguration of the large-particle sublattice with order and packing density equivalent to analogous monodisperse systems. In additive monolayers, contacts between large and small particles mutually suppress their mobility, leading to kinetic arrest far from equilibrium.<sup>32</sup>

While nonadditivity is here determined by the interfacial geometry, it can also occur in binary systems due to “soft” interactions from ligand intercalation, solvent-mediated interactions, or nanocrystal faceting, among other effects.<sup>15</sup> Under most circumstances, however, there is no straightforward correspondence between the nonadditivity and size ratio. In this geometric case, the functional relationship between  $\sigma$  and  $\Delta$  allows us to fully parameterize the monolayer’s phase behavior but also makes it challenging to disentangle their independent contributions. As shown in Figure 7a, the experimental measurements follow a path through phase space, crossing thresholds defined by eqs 3 and 4. We can test the observed behavior more generally by performing simulations of nonadditive WCA particles with constant  $\chi_s = 0.33$  and systematically varying  $\sigma$  and  $\Delta$  over a larger range of the phase space. Along  $\sigma = 1$ , nonadditivity is introduced by arbitrarily dividing the monodisperse disks into two subpopulations at separate effective heights. This condition has been previously realized experimentally, by sandwiching colloidal particles between parallel plates with variable separation.<sup>38,39</sup> The resulting simulated phase diagram is shown in Figure 7b, in which equilibrated monolayers have been classified into disordered (purple), ordered (blue), or mobile (green) phases according to threshold values of  $f_{s,hop}$  and  $|\langle \Psi_{6,L} \rangle|$ . This phase diagram, measured from simulations



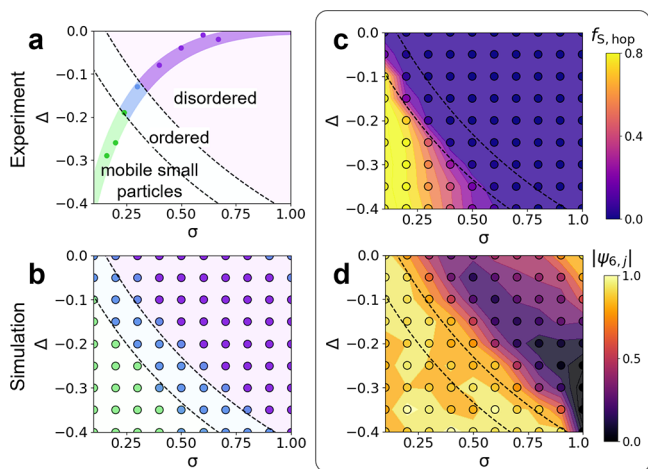


**Figure 7.** Overview of observed phase behavior. (a) Plot of the predicted phase behavior of nonadditive monolayers with varying size ratio  $\sigma$  and nonadditivity  $\Delta$ . A small-particle mobility crossover is predicted at  $(\sigma + 1)(\Delta + 1) = 1$  and a structural crossover is predicted at  $(\sigma + 1)(\Delta + 1) = 2/\sqrt{3}$ , as indicated by the dashed lines. Experimental data follows a single slice through phase space. (b) Plot of phase behavior measured from simulations of WCA particles with varying  $\sigma$  and  $\Delta$  and  $\chi_s = 0.33$ . Observed phases generally correspond with predicted crossovers. (c) Contour plots showing the small-particle hopping fraction  $f_{s,hop}$  (upper panel) and average large-particle hexagonal order  $\langle |\Psi_{6,L}| \rangle$  (lower panel) measured from each simulation. Threshold values of  $f_{s,hop} > 0.40$  for small-particle mobility and  $\langle |\Psi_{6,L}| \rangle > 0.75$  for large-particle ordering were used to determine the simulated phase behavior.

over the full range of  $\sigma$  and  $\delta$ , qualitatively agrees with both our experimental findings and our geometric predictions, capturing the three expected phase regimes of the system. Differences between the predicted phase boundaries, shown by the dashed curves, and the simulated data may be understood by considering the corresponding contour maps of small-particle mobility,  $f_{s,hop}$ , and large-particle order,  $\langle |\Psi_{6,L}| \rangle$ , shown in Figure 7c,d. In Figure 7c, small-particle hopping occurs more frequently than predicted at low  $\sigma$  because lattice dynamics create transient pathways that accommodate hops for smaller particles. Furthermore, in Figure 7d, lattice ordering with  $\langle |\Psi_{6,L}| \rangle > 0.8$  is consistently observed at values of  $\sigma$  slightly higher than predicted by the order/disorder boundary (upper dashed curve). Lattice elasticity, structural heterogeneity, and dynamic reorganization of the lattice together contribute to relax packing constraints and allow the lattice to retain hexagonal symmetry at higher size ratios than predicted. Despite not accounting for these effects, the simple geometric model successfully captures much of the observed phase behavior. Furthermore, several observations are found that are not included in this simplified representation: In regions near  $\sigma = 1$  and  $\Delta = 0$  at the top right corner of Figure 7d, a second ordered phase is formed where impurities act as substitutional defects without disrupting the lattice. Additionally, monodisperse simulations in the range  $\Delta = -0.20$  to  $-0.40$  in the lower right of Figure 7d, have low hexagonal symmetry but include regions containing ordered square lattices. This square-symmetric phase assembles to maximize the interlayer packing efficiency of confined particles at intermediate layer thicknesses.<sup>38,40</sup>

Although the experiments have examined only one slice of the accessible phase space for nonadditive binary monolayers, they highlight the importance of nonadditivity for understanding the assembled phase behavior. By modifying the surface chemistry or roughness of the particles in order to change  $\theta$ , the relationship between  $\sigma$  and  $\Delta$  could be tuned to fully explore the effects of nonadditivity. These modifications may be readily achieved following strategies used to control the wettability of colloidal particles for stabilizing emulsions.<sup>41</sup> In particular, monolayers with arbitrary  $\sigma$  and  $\Delta$  could be prepared through independent control over the contact angle of each component. Looking forward, the unique attributes of nonadditive monolayers achieved through interfacial confinement suggests a practical avenue for engineering exotic monolayer morphologies, including Kagome lattices,<sup>18,42</sup> binary superlattices,<sup>26</sup> or quasicrystals.<sup>10</sup> As these geometric assemblies do not rely on specific chemical interactions, the nanoparticle building blocks could be further functionalized to introduce desired monolayer properties. Interfacial particle assemblies have found broad utility including as surfactants for stabilizing emulsions,<sup>43</sup> catalysts for biofuel reactors,<sup>44</sup> and templates for the fabrication of nanostructured films.<sup>7</sup> The packing rules studied here for quasi-2D morphologies may also be extended to the organization of fully 3D colloidal crystals through layer-by-layer assembly.<sup>45</sup>

## CONCLUSION

Via minimally invasive electron microscopy, we have investigated the influence of nonadditivity on the phase behavior of interfacially confined bidisperse colloidal monolayers. SEM imaging of liquid droplets without encapsulation enables direct access to the ionic liquid/vacuum interface for complete tracking of particle coordinates in space and time. The interfacial attachment geometry, with large and small particle equators bound at separate vertical planes, can be naturally represented as a 2D system of nonadditive hard-disks, in which nonadditivity is determined by the mixture's size ratio. Nonadditivity is critical for understanding the observed monolayer properties, which can be classified into disordered, ordered, and mobile phase regimes. In particular, at low size ratios where nonadditivity is most significant, the monolayer exhibits small-particle transport through site-to-site hopping that would not be possible in a strictly planar, additive geometry. The structural and dynamic properties are interdependent, as the enhanced mobility of the nonadditive system facilitates equilibration of the lattice. Altogether, the observed behavior is predicted from particle packing constraints of the nonadditive geometry and is recapitulated through molecular dynamics simulations of nonadditive disks.

Looking beyond binary size mixtures of silica particles, multicomponent or heterogeneous colloidal systems may be tuned to achieve diverse and sophisticated functionality. For example, in semiconducting particle monolayers, size and spectral heterogeneity lead to exciton funneling for light-harvesting.<sup>46</sup> By virtue of using electron microscopy, one could obtain the electron beam-induced optical emission (cathodoluminescence) to demonstrate resonant energy transfer within such monolayers, collecting light emitted from some particles due to electron beam excitation of other, spectrally distinct, neighboring ones, all during monolayer evolution at an ionic liquid interface. Here, we have identified nonadditivity in colloidal mixtures as a critical ingredient for describing their assembly and phase dynamics. Although nonadditivity here is

directly determined by the binary size ratio, it is a general feature of many multicomponent systems and may arise due to ligand intercalation, particle faceting, and ionic screening, among other factors. Irrespective of its origin, control over nonadditive interactions offers a powerful and complementary strategy for tuning the properties of colloidal assemblies.

## METHODS

**Colloidal Monolayer Preparation.** Monodisperse colloidal solutions were prepared by concentrating and redispersing aqueous stock solutions of silica nanospheres with bare silanol surface chemistry (160–1000 nm diameter, 10 mg mL<sup>-1</sup>, nanocomposix) in 1-ethyl-3-methylimidazolium ethyl sulfate (EMIM<sup>+</sup>/EtSO<sub>4</sub><sup>-</sup>) ionic liquid. The monodisperse solutions had a corresponding size dispersities of 4.7% (160 nm), 8.0% (200 nm), 4.7% (300 nm), 3.8% (500 nm), and 2.2% (1000 nm). These solutions were placed in a vacuum chamber for 1 h to remove excess water. Each mixture was then prepared with a concentration of 50 mg mL<sup>-1</sup> and a 2:1 small/large number density. An additional 25 vol % glycerol was then added to each solution. We have empirically found that the addition of glycerol improves structural ordering of the resulting colloidal monolayers, potentially by reducing electrostatic screening with respect to neat IL to prevent colloidal aggregation during assembly. Next, 3  $\mu$ L droplets were deposited onto cleaned  $\sim$ 1 cm  $\times$  1 cm Si wafer substrates (Virginia Semiconductor). Substrates were cleaned by solvent rinses with isopropyl alcohol, acetone, and distilled water followed by 2 min O<sub>2</sub> plasma cleaning. Prior to imaging, droplets were stored under an inert N<sub>2</sub> environment for at least 12 h to allow for monolayer equilibration.

**Scanning Electron Microscopy.** Droplets on Si wafers were grounded with a copper clip and loaded into the chamber of a Zeiss Gemini SUPRA 55 S2 SEM. Imaging was performed using an accelerating voltage of 3 keV and a beam current of  $15 \pm 2$  pA. Each SEM movie and image was acquired at a new sample region to mitigate the effects of beam exposure. The beam dose, which depended on the size of the imaging field of view, was varied over a range of  $5\text{--}16\text{ e}^- \text{ nm}^{-2} \text{ s}^{-1}$ .

**Single Particle Tracking and Analysis.** SEM data were analyzed with custom python code. Individual particles were identified from image data using a Laplacian of Gaussians filter, with particle sizes determined from the standard deviation of each feature. From measurement of stationary colloidal lattices, we estimate a center positional uncertainty of 25 nm. Following automated size classification, binary particle assignments were manually confirmed for each image. Features from each frame were linked into time-dependent trajectories using the trackpy package, which implements the Crocker–Grier algorithm.<sup>47</sup> Trajectories were drift corrected using the large-particle sublattice as a stable reference.

**Molecular Dynamics Simulations.** Molecular dynamics simulations of binary particles with variable size ratio and nonadditivity were conducted using LAMMPS.<sup>48</sup> Each simulation was performed in two dimensions with periodic boundary conditions. Particle interactions were described using a WCA potential to produce a steep short-range repulsion, and nonadditivity was incorporated by shortening the WCA interaction length scale for large-small interactions. Simulations were carried out in Lennard–Jones units, with the fundamental time step determined from the diffusive time scale of the large particles. To ensure consistent particle density across the range of size ratios, simulations were performed in the isothermal–isobaric ensemble in a flexible simulation box, using a Langevin thermostat to maintain constant temperature and a Nosé–Hoover barostat to maintain constant pressure. Constant pressure conditions reflect our experiments where the imaging field of view is surrounded by a dense network of particles. For each size ratio, the initial conditions were determined for a system of 900 particles with a number fraction of  $\chi_s = 0.33$  by steadily increasing the system pressure to its final equilibrium value of  $P = 0.1$  in reduced Lennard–Jones units. Following initialization, we confirm equilibration by

verifying constant system properties and dynamics independent of the sampling time.

## ASSOCIATED CONTENT

### Supporting Information

The Supporting Information is available free of charge at <https://pubs.acs.org/doi/10.1021/acsnano.2c12668>.

Discussions of the effects of beam perturbation, analysis of the dependence of the SEM accelerating voltage on particle imaging, derivation of the relevant dynamic time scale for small-particle transport, analysis of the packing of monodisperse assemblies, procedure for generating small-particle distribution maps, and the effects of interparticle attraction on molecular dynamics simulations and figures of SEM images, Gaussian kernel density estimation of the small-particle positions, symmetrized density distribution, and comparison of small-particle distributions between experiment and simulation (PDF)

## AUTHOR INFORMATION

### Corresponding Author

Naomi S. Ginsberg – Department of Chemistry, University of California, Berkeley, California 94720, United States; Department of Physics, University of California, Berkeley, California 94720, United States; Molecular Biophysics and Integrated Bioimaging Division and Materials Sciences Division, Lawrence Berkeley National Laboratory, Berkeley, California 94720, United States; Kavli Energy NanoScience Institute, Berkeley, California 94720, United States; STROBE, NSF Science & Technology Center, Berkeley, California 94720, United States; [orcid.org/0000-0002-5660-3586](https://orcid.org/0000-0002-5660-3586); Email: [nsginsberg@berkeley.edu](mailto:nsginsberg@berkeley.edu)

### Authors

Jonathan G. Raybin – Department of Chemistry, University of California, Berkeley, California 94720, United States; [orcid.org/0000-0001-9040-4241](https://orcid.org/0000-0001-9040-4241)  
Rebecca B. Wai – Department of Chemistry, University of California, Berkeley, California 94720, United States; [orcid.org/0000-0001-6944-2235](https://orcid.org/0000-0001-6944-2235)

Complete contact information is available at: <https://pubs.acs.org/doi/10.1021/acsnano.2c12668>

### Notes

The authors declare no competing financial interest.

## ACKNOWLEDGMENTS

The authors thank A. Das for valuable discussions and input on simulations and A. Omar for helpful comments on the manuscript. The authors thank E. Wong, E. S. Barnard, D. F. Ogletree, and S. Aloni at the Molecular Foundry for assistance with SEM. This work was supported by STROBE, A National Science Foundation Science & Technology Center under Grant No. DMR 1548924. The SEM imaging at the Lawrence Berkeley Lab Molecular Foundry was performed as part of the Molecular Foundry user program, supported by the Office of Science, Office of Basic Energy Sciences, of the U.S. Department of Energy under Contract No. DE-AC02-05CH11231. R.B.W. acknowledges a NSF Graduate Research Fellowships (No. DGE1106400), and N.S.G. acknowledges an Alfred P. Sloan Research Fellowship, a David and Lucile



Packard Foundation Fellowship for Science and Engineering, and a Camille and Henry Dreyfus Teacher-Scholar Award.

## REFERENCES

- (1) Boles, M. A.; Engel, M.; Talapin, D. V. Self-Assembly of Colloidal Nanocrystals: From Intricate Structures to Functional Materials. *Chem. Rev.* **2016**, *116*, 11220–11289.
- (2) Manoharan, V. N. Colloidal matter: Packing, geometry, and entropy. *Science* **2015**, *349*, 1253751.
- (3) Thornework, A. L.; Schnyder, S. K.; Aarts, D. G. A. L.; Horbach, J.; Roth, R.; Dullens, R. P. A. Structure factors in a two-dimensional binary colloidal hard sphere system. *Mol. Phys.* **2018**, *116*, 3245–3257.
- (4) van der Meer, B.; Lathouwers, E.; Smalenburg, F.; Filion, L. Diffusion and interactions of interstitials in hard-sphere interstitial solid solutions. *J. Chem. Phys.* **2017**, *147*, 234903.
- (5) Cho, Y.-S.; Yi, G.-R.; Lim, J.-M.; Kim, S.-H.; Manoharan, V. N.; Pine, D. J.; Yang, S.-M. Self-Organization of Bidisperse Colloids in Water Droplets. *J. Am. Chem. Soc.* **2005**, *127*, 15968–15975.
- (6) Dong, A.; Ye, X.; Chen, J.; Murray, C. B. Two-Dimensional Binary and Ternary Nanocrystal Superlattices: The Case of Monolayers and Bilayers. *Nano Lett.* **2011**, *11*, 1804–1809.
- (7) Lotito, V.; Zambelli, T. Approaches to self-assembly of colloidal monolayers: A guide for nanotechnologists. *Adv. Colloid Interface Sci.* **2017**, *246*, 217–274.
- (8) Talapin, D. V.; Shevchenko, E. V.; Bodnarchuk, M. I.; Ye, X.; Chen, J.; Murray, C. B. Quasicrystalline order in self-assembled binary nanoparticle superlattices. *Nature* **2009**, *461*, 964–967.
- (9) Ye, X.; Chen, J.; Eric Irrgang, M.; Engel, M.; Dong, A.; Glotzer, S. C.; Murray, C. B. Quasicrystalline nanocrystal superlattice with partial matching rules. *Nat. Mater.* **2017**, *16*, 214–219.
- (10) Fayen, E.; Impéror-Clerc, M.; Filion, L.; Foffi, G.; Smalenburg, F. Self-assembly of dodecagonal and octagonal quasicrystals in hard spheres on a plane. *Soft Matter* **2023**, *19*, 2654–2663.
- (11) Gao, Y.; Kim, P. Y.; Hoagland, D. A.; Russell, T. P. Bidisperse Nanospheres Jammed on a Liquid Surface. *ACS Nano* **2020**, *14*, 10589–10599.
- (12) Filion, L.; Dijkstra, M. Prediction of binary hard-sphere crystal structures. *Phys. Rev. E* **2009**, *79*, 046714.
- (13) Fayen, E.; Jagannathan, A.; Foffi, G.; Smalenburg, F. Infinite-pressure phase diagram of binary mixtures of (non)additive hard disks. *J. Chem. Phys.* **2020**, *152*, 204901.
- (14) Dijkstra, M. Phase behavior of nonadditive hard-sphere mixtures. *Phys. Rev. E* **1998**, *58*, 7523–7528.
- (15) Silveira Batista, C. A.; Larson, R. G.; Kotov, N. A. Nonadditivity of nanoparticle interactions. *Science* **2015**, *350*, 1242477.
- (16) Binder, K.; Virnau, P.; Statt, A. Perspective: The Asakura Oosawa model: A colloid prototype for bulk and interfacial phase behavior. *J. Chem. Phys.* **2014**, *141*, 140901.
- (17) Widmer-Cooper, A.; Harrowell, P. Structural phases in non-additive soft-disk mixtures: Glasses, substitutional order, and random tilings. *J. Chem. Phys.* **2011**, *135*, 224515.
- (18) Salgado-Blanco, D.; Mendoza, C. I. Non-additive simple potentials for pre-programmed self-assembly. *Soft Matter* **2015**, *11*, 889–897.
- (19) Baumgartl, J.; Dullens, R. P. A.; Dijkstra, M.; Roth, R.; Bechinger, C. Experimental Observation of Structural Crossover in Binary Mixtures of Colloidal Hard Spheres. *Phys. Rev. Lett.* **2007**, *98*, 198303.
- (20) Ebert, F.; Maret, G.; Keim, P. Partial clustering prevents global crystallization in a binary 2D colloidal glass former. *Eur. Phys. J. E* **2009**, *29*, 311–318.
- (21) Mazoyer, S.; Ebert, F.; Maret, G.; Keim, P. Dynamics of particles and cages in an experimental 2D glass former. *EPL (Europhysics Letters)* **2009**, *88*, 66004.
- (22) Bonales, L. J.; Martínez-Pedrero, F.; Rubio, M. A.; Rubio, R. G.; Ortega, F. Phase Behavior of Dense Colloidal Binary Monolayers. *Langmuir* **2012**, *28*, 16555–16566.
- (23) Thornework, A. L.; Roth, R.; Aarts, D. G. A. L.; Dullens, R. P. A. Communication: Radial distribution functions in a two-dimensional binary colloidal hard sphere system. *J. Chem. Phys.* **2014**, *140*, 161106.
- (24) Thornework, A. L.; Aarts, D. G. A. L.; Horbach, J.; Dullens, R. P. A. Self-diffusion in two-dimensional binary colloidal hard-sphere fluids. *Phys. Rev. E* **2017**, *95*, 012614.
- (25) Lavergne, F. A.; Diana, S.; Aarts, D. G. A. L.; Dullens, R. P. A. Equilibrium Grain Boundary Segregation and Clustering of Impurities in Colloidal Polycrystalline Monolayers. *Langmuir* **2016**, *32*, 12716–12724.
- (26) Zhou, Y.; Arya, G. Discovery of two-dimensional binary nanoparticle superlattices using global Monte Carlo optimization. *Nat. Commun.* **2022**, *13*, 7976.
- (27) Bischak, C. G.; Raybin, J. G.; Kruppe, J. W.; Ginsberg, N. S. Charging-driven coarsening and melting of a colloidal nanoparticle monolayer at an ionic liquid–vacuum interface. *Soft Matter* **2020**, *16*, 9578–9589.
- (28) Kim, P. Y.; Gao, Y.; Chai, Y.; Ashby, P. D.; Ribbe, A. E.; Hoagland, D. A.; Russell, T. P. Assessing Pair Interaction Potentials of Nanoparticles on Liquid Interfaces. *ACS Nano* **2019**, *13*, 3075–3082.
- (29) Kim, P. Y.; Ribbe, A. E.; Russell, T. P.; Hoagland, D. A. Visualizing the Dynamics of Nanoparticles in Liquids by Scanning Electron Microscopy. *ACS Nano* **2016**, *10*, 6257–6264.
- (30) Weeks, J. D.; Chandler, D.; Andersen, H. C. Role of Repulsive Forces in Determining the Equilibrium Structure of Simple Liquids. *J. Chem. Phys.* **1971**, *54*, 5237–5247.
- (31) Hunter, G. L.; Weeks, E. R. The physics of the colloidal glass transition. *Rep. Prog. Phys.* **2012**, *75*, 066501.
- (32) Cui, M.; Miesch, C.; Kosif, I.; Nie, H.; Kim, P. Y.; Kim, H.; Emrick, T.; Russell, T. P. Transition in Dynamics as Nanoparticles Jam at the Liquid/Liquid Interface. *Nano Lett.* **2017**, *17*, 6855–6862.
- (33) Likos, C. N.; Henley, C. L. Complex alloy phases for binary hard-disc mixtures. *Philosophical Magazine B* **1993**, *68*, 85–113.
- (34) Koeze, D. J.; Vågberg, D.; Tjoo, B. B. T.; Tighe, B. P. Mapping the jamming transition of bidisperse mixtures. *EPL (Europhysics Letters)* **2016**, *113*, 54001.
- (35) Tauber, J.; Higler, R.; Sprakel, J. Anomalous dynamics of interstitial dopants in soft crystals. *Proc. Natl. Acad. Sci. U. S. A.* **2016**, *113*, 13660–13665.
- (36) König, H.; Hund, R.; Zahn, K.; Maret, G. Experimental realization of a model glass former in 2D. *Eur. Phys. J. E* **2005**, *18*, 287–293.
- (37) Zaccone, A. Explicit Analytical Solution for Random Close Packing in  $d = 2$  and  $d = 3$ . *Phys. Rev. Lett.* **2022**, *128*, 028002.
- (38) Pieranski, P. Two-Dimensional Interfacial Colloidal Crystals. *Phys. Rev. Lett.* **1980**, *45*, 569–572.
- (39) Han, Y.; Shokef, Y.; Alsayed, A. M.; Yunker, P.; Lubensky, T. C.; Yodh, A. G. Geometric frustration in buckled colloidal monolayers. *Nature* **2008**, *456*, 898–903.
- (40) Curk, T.; de Hoogh, A.; Martínez-Veracoechea, F. J.; Eiser, E.; Frenkel, D.; Dobnikar, J.; Leunissen, M. E. Layering, freezing, and re-entrant melting of hard spheres in soft confinement. *Phys. Rev. E* **2012**, *85*, 021502.
- (41) Xiao, M.; Xu, A.; Zhang, T.; Hong, L. Tailoring the Wettability of Colloidal Particles for Pickering Emulsions via Surface Modification and Roughness. *Front. Chem.* **2018**, *6*, 225.
- (42) Chen, Q.; Bae, S. C.; Granick, S. Directed self-assembly of a colloidal kagome lattice. *Nature* **2011**, *469*, 381–384.
- (43) Shi, S.; Russell, T. P. Nanoparticle Assembly at Liquid–Liquid Interfaces: From the Nanoscale to Mesoscale. *Adv. Mater.* **2018**, *30*, 1800714.
- (44) Crossley, S.; Faria, J.; Shen, M.; Resasco, D. E. Solid Nanoparticles that Catalyze Biofuel Upgrade Reactions at the Water/Oil Interface. *Science* **2010**, *327*, 68–72.
- (45) Velikov, K. P.; Christova, C. G.; Dullens, R. P. A.; van Blaaderen, A. Layer-by-Layer Growth of Binary Colloidal Crystals. *Science* **2002**, *296*, 106–109.

(46) Nguyen, D.; Nguyen, H. A.; Lyding, J. W.; Gruebele, M. Imaging and Manipulating Energy Transfer Among Quantum Dots at Individual Dot Resolution. *ACS Nano* **2017**, *11*, 6328–6335.

(47) Crocker, J. C.; Grier, D. G. Methods of Digital Video Microscopy for Colloidal Studies. *J. Colloid Interface Sci.* **1996**, *179*, 298–310.

(48) Thompson, A. P.; Aktulga, H. M.; Berger, R.; Bolintineanu, D. S.; Brown, W. M.; Crozier, P. S.; in 't Veld, P. J.; Kohlmeyer, A.; Moore, S. G.; Nguyen, T. D.; Shan, R.; Stevens, M. J.; Tranchida, J.; Trott, C.; Plimpton, S. J. LAMMPS - a flexible simulation tool for particle-based materials modeling at the atomic, meso, and continuum scales. *Comput. Phys. Commun.* **2022**, *271*, 108171.

## Recommended by ACS

### Capillary Assembly of Anisotropic Particles at Cylindrical Fluid–Fluid Interfaces

Jack L. Eatson, D. Martin A. Buzza, *et al.*

APRIL 18, 2023  
LANGMUIR

READ 

### Rotational Dynamics of Discoid Colloidal Particles in Attractive Quasi-Two-Dimensional Plastic Crystals

Bing Liu, An-Chang Shi, *et al.*

MARCH 01, 2023  
THE JOURNAL OF PHYSICAL CHEMISTRY LETTERS

READ 

### Connecting Colloidal Forces to the Equilibrium Thickness of Particulate Deposits on a Substrate in Contact with a Suspension Using Classical Density Functional Theory

Roi Bar-On and Ofer Manor

APRIL 10, 2023  
LANGMUIR

READ 

### Engineering the Thermodynamic Stability and Metastability of Mesophases of Colloidal Bipyramids through Shape Entropy

Yein Lim, Sharon C. Glotzer, *et al.*

FEBRUARY 28, 2023  
ACS NANO

READ 

Get More Suggestions >